Joule

CellPress

Article

Impact of the valence band energy alignment at the hole-collecting interface on the photostability of wide band-gap perovskite solar cells

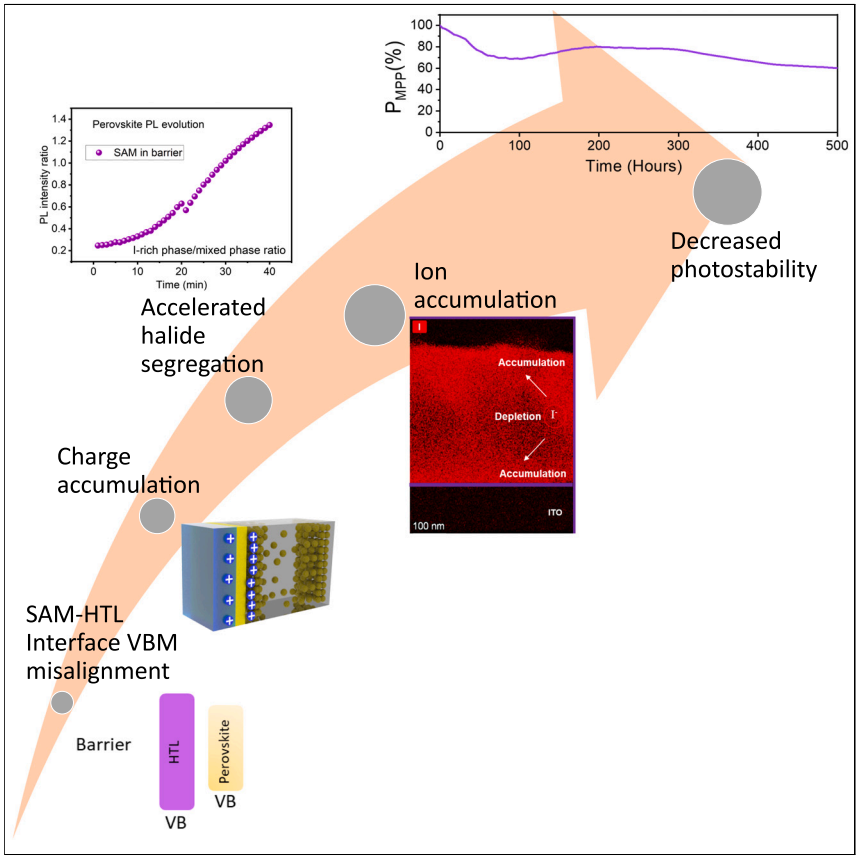

The rapid growth of attention from the photovoltaics (PV) industry to perovskite-based multijunction (MJ) PV to reduce the levelized cost of energy motivates the scientific community to accelerate the study of the remaining bottlenecks to commercialize this PV technology. In this regard, the photostability of the wide band-gap (WBG) perovskite used in this MJ-PV remains a major impediment to the increased lifetime of perovskite-based MJ-PV. Here, we present a systematic study to maximize the photostability of WBG perovskite solar cells.

Luis Victor Torres Merino, Christopher E. Petoukhoff, Oleksandr Matiash, ..., Martin Stolterfoht, Frédéric Laquai, Stefaan De Wolf

luis.torresmerino@kaust.edu.sa (L.V.T.M.)
stefaan.dewolf@kaust.edu.sa (S.D.W.)

Highlights

Influence of VBM alignment at the HTL/perovskite interface on charge accumulation

Interface-altered electric fields accelerate halide segregation

Blending SAMs to customize HTL's VBM

PL evolution qualitatively predicts WBG PSC photostability through halide segregation

Torres Merino et al., Joule *8*, 1–22
September 18, 2024
https://doi.org/10.1016/j.joule.2024.06.017

Please cite this article in press as: Torres Merino et al., Impact of the valence band energy alignment at the hole-collecting interface on the photostability of wide band-gap perovskite solar cells, Joule (2024), https://doi.org/10.1016/j.joule.2024.06.017

Joule

CellPress

Article

Impact of the valence band energy alignment at the hole-collecting interface on the photostability of wide band-gap perovskite solar cells

Luis Victor Torres Merino,[1,*] Christopher E. Petoukhoff,[1] Oleksandr Matiash,[1] Anand Selvin Subbiah,[1] Carolina Villamil Franco,[1] Pia Dally,[1] Badri Vishal,[1] Sofiia Kosar,[1] Diego Rosas Villalva,[1] Vladyslav Hnapovskyi,[1] Esma Ugur,[1] Sahil Shah,[2] Francisco Peña Camargo,[2] Orestis Karalis,[3] Hannes Hempel,[3] Igal Levine,[3] Rakesh R. Pradhan,[1] Suzana Kralj,[4] Nikhil Kalasariya,[5] Maxime Babics,[1] Bumin Kagan Yildirim,[1] Ahmed A. Said,[1] Erkan Aydin,[1] Helen Bristow,[1] Subhashri Mannar,[1] Waseem Raja,[1] Anil Reddy Pininti,[1] Adi Prasetio,[1] Arsalan Razzaq,[1] Hamza Al Nasser,[1] Thomas G. Allen,[1] Furkan H. Isikgor,[1] Derya Baran,[1] Thomas D. Anthopoulos,[1] Monica Morales Masis,[4] Udo Schwingenschlögl,[1] Thomas Unold,[3] Martin Stolterfoht,[2,5] Frédéric Laquai,[1] and Stefaan De Wolf[1,6,*]

SUMMARY

This work discusses the need to enhance charge carrier collection to minimize halide segregation in wide band-gap (WBG) perovskites. Here, we systematically elucidate the impact of valence band maximum (VBM) offsets and energetic barriers formed at the hole transport layer (HTL)/perovskite interface on charge accumulation, its influence on halide segregation, and ultimately on perovskite solar cell (PSC) long-term photostability. To this end, we precisely tune the VBM-HTL energetic levels by employing blends of self-assembled monolayers (SAMs; MeO-2PACz and Br-2PACz) to fabricate customized HTLs for PSCs with three different WBG perovskite photoabsorbers (1.69, 1.81, and 2.00 eV), commonly used in various tandem configurations. We find that optimized energetic alignment at the SAM HTL/perovskite interface significantly enhances the long-term photostability of the WBG PSCs. Our results show that photostability of devices can be predicted when comparing HTL/perovskite interfaces using photoluminescence's evolution and transient surface photovoltage spectroscopies of half-stacks (glass/metal oxide/HTL/perovskite) in correlation with halide segregation.

INTRODUCTION

Perovskite-based multijunction photovoltaics (PVs) are attracting widespread attention from academia and industry due to their demonstrated high power conversion efficiency (PCE) and promise of low-cost manufacturing.[1–5] Yet, performance degradation remains a major impediment to the commercialization of this technology.[4–7] The wide band-gap (WBG) perovskites used as top cell absorbers in tandems are of particular concern due to photo-induced segregation of the mixed-halide (bromide/iodide) perovskite phase into iodide and bromide-rich domains.[6,8–11] Once such segregation occurs, charge carriers can funnel to the created iodide-rich phases with a narrower band gap, reducing overall device performance and stability.[11–15]

CONTEXT & SCALE

Halide segregation in wide band-gap halide perovskites is an important bottleneck toward long operational lifetimes of perovskite-based multijunction solar cells. To minimize this phenomenon, aside from other well-known strategies such as perovskite defect passivation, enhancing the charge carrier collection needs to be effectively addressed. Here, we report a universal method to improve the hole collection in *p-i-n* perovskite solar cells (PSCs) by engineering the energetic alignment between the perovskite and the hole-selective contact through blended SAMs, MeO-2PACz with Br-2PACz. With the presented correlation between carrier collection and halide segregation analysis in this study, we show that it is possible to predict which interface is less prone to promote halide segregation, and thus it can be used to accelerate the development of PSCs with increased photostability. By

Please cite this article in press as: Torres Merino et al., Impact of the valence band energy alignment at the hole-collecting interface on the photostability of wide band-gap perovskite solar cells, Joule (2024), https://doi.org/10.1016/j.joule.2024.06.017

It is thus essential to formulate effective strategies to minimize halide phase segregation to increase the operational lifetime of WBG perovskite-based PVs.[16]

So far, approaches toward reducing halide segregation in WBG perovskites have centered around defect passivation and enhanced carrier extraction strategies.[6] Defect-assisted photo-induced halide segregation is a common phenomenon in WBG perovskites, where many passivation studies aim to reduce the bulk and surface defect density of the WBG absorber to suppress halide segregation.[17] In addition to compositional dependencies, surface and bulk defect densities as well as mobile ion densities may vary drastically under light stress, i.e., upon charge generation in the perovskite absorber.[5,6,8,16–19] Carrier extraction, on the other hand, depends on various parameters such as each of the transport layer's carrier mobility, its thickness, the charge extraction velocity, and overall interface energetics.[18,19] The latter also dictates the charge extraction selectivity (holes versus electrons) and minimizes interface recombination through energetic barriers or by inducing an internal electrical field.[6,9,19–21] In the *p-i-n* configuration of perovskite solar cells (PSCs), the *p*-type hole transport layer (HTL) is first deposited, followed by the intrinsic perovskite absorber (*i*), and then the *n*-type electron transport layer (ETL). In *p-i-n* devices, for the perovskite/ETL top interface, 2D perovskites and thin insulating materials are nowadays often employed to passivate the surface, prevent hole injection, and enhance electron extraction.[18,22–25] As for the HTL/perovskite bottom interface of *p-i-n* devices, enhanced hole extraction is known to decelerate halide segregation in the bulk perovskite due to a decrease in interfacial recombination.[6,9,22,26–28]

The success of the recently emerged phosphonic acid-based self-assembled monolayers (SAMs), usually anchored on a transparent conductive oxide (TCO), as promising HTLs in *p-i-n* PSCs has been primarily ascribed to their passivation of the perovskite and fast hole extraction, in comparison with conventional HTLs such as poly(3,4-ethylenedioxythiophene) polystyrene sulfonate (PEDOT:PSS), poly(triaryl amine) (PTAA), or nickel oxide (NiO_x).[27–30] The fast hole extraction of these SAMs likely stems from a combination of a low series resistance due to their minimal thickness, interface passivation, and well-aligned valence band maximum (SAM_{VBM}) with that of the perovskite (PVK_{VBM}) (i.e., with minimal energetic mismatch for hole extraction).[22,27–29,31] Besides such well-matched properties, the class of molecular SAMs additionally features a much broader materials design space compared with their conventional HTL counterparts,[32] offering further opportunities for improving device performance and stability. For this, different types of SAM molecules may be required for optimal device performance when using different perovskite compositions.[27,28,31–35] Yet, despite studies reporting indium-tin oxide (ITO)/SAM/perovskite being a near lossless interface, a clear rationale behind the choice of a given SAM for distinct perovskite compositions with specific band gaps remains missing, especially in terms of linking optimal energetic alignment, passivation, suppression of phase segregation, and, ultimately, device stability. To this end, it is crucial to disentangle the effect of HTL/perovskite interface passivation from energy-matching requirements to gain insight into the limiting physical process and to provide a universal strategy to decelerate halide segregation.

This work employs commercially available SAM molecules with distinct dipole moments, MeO-2PACz, Me-4PACz, 2PACz, Br-2PACz, and the mixture of MeO-2PACz and Br-2PACz (MeO:Br)-2PACz in different molar ratios. To ensure an energetically finely matched SAM_{VBM}/PVK_{VBM} interface, we used specific (MeO:Br)-2PACz compositions with molar ratios of 70:30, 50:50, and 40:60 for the 1.69, 1.81, and 2.00 eV WBG PSCs, respectively. We note that all three WBG compositions

studying different perovskite compositions, we highlight the universality of our method.

[1]King Abdullah University of Science and Technology (KAUST), Physical Sciences and Engineering Division (PSE), KAUST Solar Center (KSC), Thuwal 23955-6900, Saudi Arabia

[2]Institute of Physics and Astronomy, University of Potsdam, Golm, 14476 Potsdam, Germany

[3]Helmholtz-Zentrum Berlin, 12489 Berlin, Germany

[4]MESA+ Institute for Nanotechnology, University of Twente, 7522 NB Enschede, the Netherlands

[5]Department of Electronic Engineering, The Chinese University of Hong Kong, 999077 Hong Kong, China

[6]Lead contact

*Correspondence: luis.torresmerino@kaust.edu.sa (L.V.T.M.), stefaan.dewolf@kaust.edu.sa (S.D.W.)

https://doi.org/10.1016/j.joule.2024.06.017

Please cite this article in press as: Torres Merino et al., Impact of the valence band energy alignment at the hole-collecting interface on the photostability of wide band-gap perovskite solar cells, Joule (2024), https://doi.org/10.1016/j.joule.2024.06.017

employed in spin-coated PSCs were intentionally kept pristine (i.e., without employing additional bulk or interfacial passivation strategies) to highlight the role of the HTL/perovskite interface in increasing the PSC long-term photostability. The studied perovskites are of interest for a wide variety of multijunction perovskite solar cells, such as monolithic double junction (2-J, two active layers) perovskite/silicon[36,37]; perovskite/perovskite[38] and perovskite/organic[22,39]; and triple junction (3-J, three active layers) all perovskite,[40] perovskite/perovskite/organic,[41] and perovskite/perovskite/silicon[42] tandems, respectively.

Based on these empirical results and computational simulations elucidating the impact of the charge carrier density and mobile ion density at the HTL/perovskite interface, we propose a model to explain the decelerated phase segregation with (MeO:Br)-2PACz as the HTL. Overall, this work highlights the importance of SAM_{VBM}/PVK_{VBM} energetic alignment for enhanced hole collection to minimize phase segregation in WBG perovskites, leading to extended photostability in PSCs. We further show that a fast test on photoluminescence evolution and transient surface photovoltage (Tr-SPV) spectroscopies can predict qualitatively the photostability of WBG PSCs, which is a methodology that can be used to accelerate the development of perovskite-based tandems with increased operational lifetimes.

RESULTS

The choice of SAM molecules

First, we identified three technologically relevant perovskite band gaps (namely 1.69, 1.81, and 2.00 eV) that may find applications in current-matched monolithic 2-J (Figure S1A) and 3-J tandems (Figure S1B) under standard test conditions (AM1.5G spectrum, 1 sun intensity, 25°C, Figure S1). To obtain the targeted WBG perovskites for spin-coated PSCs, we employed a perovskite ink formulation with a commonly used double cation composition, $FA_{0.83}Cs_{0.17}Pb(Br_XI_{1-X})_3$. By changing the $Br_{(X)}/(I_{(1-X)} + Br_{(X)})$ ratios (Figure S2) to 0.3, 0.5, and 0.7, we then obtained the three targeted band gaps (corresponding to 1.69, 1.81, and 2.00 eV, extracted from the Tauc plots, Figure S2). The perovskite ionization energy, PVK_{VBM}, of three perovskite layers was then measured using ultraviolet photoelectron spectroscopy (UPS) and photoelectron spectroscopy in air (PESA) (Figure 1A, S3, and S4). Similarly, the conduction band minimum (CBM) and work function (WF) of the perovskite layers were estimated from UPS and inverse photoelectron spectroscopy (IPES) in vacuum (Figure S3). UPS and PESA measurements show that the ionization energies of perovskites shift toward slightly higher values (5.43–5.73 eV [UPS] and 5.44–5.59 eV [PESA]), with increasing band gap from 1.69 to 2.00 eV.

Considering the obtained PVK_{VBM}, we explore four well-known phosphonic-acid-based SAM molecules, MeO-2PACz, Br-2PACz, Me-4PACz, and the commonly used 2PACz as a SAM-based HTL for *p-i-n* PSCs (Figure 1B). Figure 1C shows the chemical structure of the molecules and the water-contact angles measured for the SAM layers on glass/ITO substrates. UPS and PESA measurements reveal similar ionization energies measured for these SAMs on glass/ITO substrates (Figures 1A and S5–S7), which align well with the highest occupied molecular orbital (HOMO) values from density functional theory (DFT) calculations (Figures 1A and 1D). We also note similarities in ionization energies within molecules from DFT and PESA when measuring glass/powder samples (Figures 1D, S8, and S9). Table S1 summarizes the ionization energies obtained for all four SAM molecules using different techniques and DFT calculations. Although the ionization energy of Me-4PACz (~5.50 eV) aligns well with the PVK_{VBM} values, its hydrophobic nature leads to

Please cite this article in press as: Torres Merino et al., Impact of the valence band energy alignment at the hole-collecting interface on the photostability of wide band-gap perovskite solar cells, Joule (2024), https://doi.org/10.1016/j.joule.2024.06.017

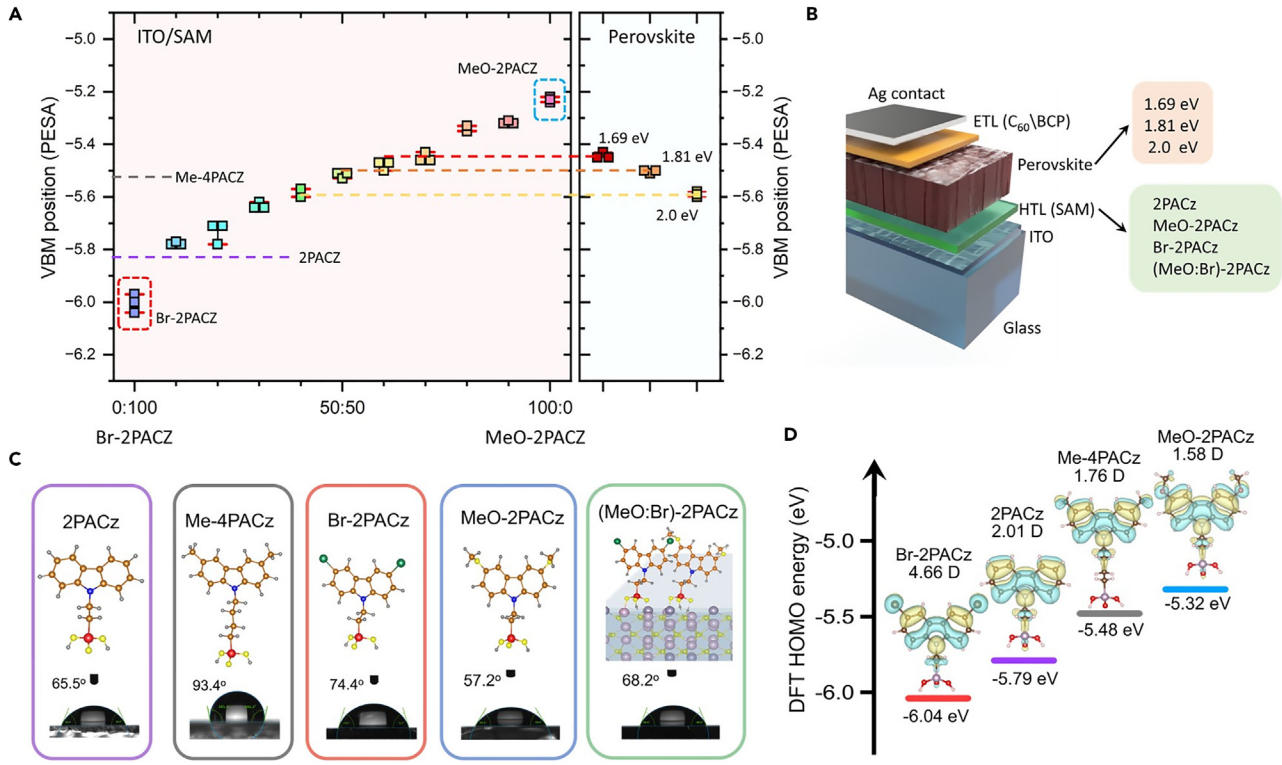

Figure 1. Energy alignment of the perovskites and SAMs films

(A) Valence band maximum (VBM) of SAM HTLs and perovskites, measured by PESA.

(B) Material stack for the device architecture used in this work.

(C) Chemical structure of SAM molecules and their water-contact angle.

(D) HOMO energy of SAM molecules calculated with DFT.

poor surface coverage of perovskite-precursor solutions (Figure S10). On the other hand, the widely used 2PACz, although relatively less hydrophobic, appears to introduce a hole extraction barrier for any of the perovskite films under study due to its high ionization energy (~5.81 eV, Figure 1A). The ionization energies of Br-2PACz (6.0 eV) and MeO-2PACz (5.23 eV) derivatives represent the upper and lower bounds, respectively, of our PVK_{VBM} films (Figure 1A), and by mixing them in fixed molar ratios, we can tune monotonically the ionization energy of the (MeO:Br)-2PACz blend between such bound values (Figures 1A and S11), enabling suitable energy alignment. The blends also offer a relatively less hydrophobic layer than Me-4PACz (Figure 1C).

To best match the PVK_{VBM} values (Figures S3 and S4), we mixed both SAM molecules (MeO-2PACz and Br-2PACz) in various molar ratios ((MeO:Br)-2PACz) and performed a linear regression fit between the measured individual SAM_{VBM} values (Figures 1A and S11). Based on these data, we fixed the molar ratio of (MeO:Br)-2PACz for each perovskite band gap to be (70:30) for 1.69 eV, (50:50) for 1.81 eV, and (40:60) for 2.00 eV, enabling SAM_{VBM}/PVK_{VBM} matching. Kelvin probe force microscopy (KPFM) measurements show the lateral homogeneity of the HTLs with a uniform potential distribution across the surface (Figure S12) for MeO-2PACz, Br-2PACz, and (MeO:Br)-2PACz films on ITO. We then calculated the WF for each film and found that the (50:50) (MeO:Br)-2PACz blend lies exactly in between MeO-2PACz and Br-2PACz (Figure S13; Table S2). The scanning electron microscopy (SEM) images (Figures S14 and S15) reveal only a minimal morphological

difference for WBG perovskites fabricated on top of MeO-2PACz, Br-2PACz, (MeO:Br)-2PACz, and 2PACz layers, in agreement with previous reports.[27,28,31] X-ray diffraction (XRD) patterns (with a point detector) of the WBG perovskites show variations between different HTL substrates, especially for the 1.69 eV perovskite (Figure S16). To provide a more thorough analysis on perovskite crystal formation upon distinct SAMs, we performed further XRD analysis through grazing-incidence wide-angle X-ray scattering (GIWAXS) (with a 2D detector) to investigate more precisely if such possible crystal differences significantly influence the spectroscopy, performance, and photostability of our samples.[43–45] These GIWAXS results will be discussed in the last section, where we provide a holistic approach to our proposed mechanism model.

The quasi-Fermi level splitting (QFLS) of the three perovskites in the half-device stack (glass/ITO/HTL/perovskite) was calculated from hyperspectral PL imaging measurements (Figure S17). The QFLS changes for each perovskite band gap with distinct SAM layers as HTL were minimal, as shown in Figures 2A and S17 and Table S3. We further measured the transient absorption (TA) response on the half-device stacks (Figures S18–S21; Notes S1 and S2) to monitor the photobleach (PB) signal and to gain insight into the hole transfer at the ITO/HTL/perovskite interface, with each different SAM. For all 3 perovskites, the lifetime of the PB signals was reduced for the ITO/HTL/perovskite stacks compared with the neat perovskite PB lifetimes. This reduced lifetime can arise from either charge transfer (CT) to the ITO/HTL layer or interfacial recombination. To disentangle these two competing kinetic processes, we calculated a differential lifetime (t_{diff}), using the equation:

$$t_{diff} = -\left\{\frac{dln\left(\frac{\Delta T}{T_n}\right)}{dT}\right\}^{-1} \quad \text{(Equation 1)}$$

where $\Delta T/T_n$ is the normalized PB signal as a function of pump-probe delay time (Figure 2B). This approach has been previously used for time-resolved photoluminescence (TRPL) experiments to separate processes that occur over very different timescales.[27,46–48] CT can be assigned to the fast timescales, in which t_{diff} is rapidly rising, whereas interfacial recombination can be assigned to the longer time scales, in which t_{diff} reaches a plateau (t_{sat}). Lower values of t_{sat}, particularly when t_{sat} is significantly reduced relative to the bulk perovskite lifetime (t_{bulk}), indicate a greater degree of interfacial recombination. Thus, interfacial recombination dominates for the 1.69 and 2.00 eV perovskites, since t_{sat} is significantly reduced compared with t_{bulk}. For example, for the MeO-2PACz/1.69 eV perovskite, t_{sat} was 3.35 ns, compared with t_{bulk} of 10 ns.

Hole transfer from the perovskite to the ITO/SAM layer was monitored by tracking the slope of the hole transfer regime (S_{CT}) and the time when CT was complete (t_{CT}). Generally, the SAMs with energy-level offset (i.e., MeO-2PACz) or aligned (i.e., (MeO:Br)-2PACz) had faster hole transfer rates: for the 1.69 eV perovskite, MeO-2PACz and (MeO:Br)-2PACz had S_{CT} of 4.07 and 2.97, compared with 1.44 and 1.22 for Br-2PACz and 2PACz. Additionally, they had shorter t_{CT}: MeO-2PACz and (MeO:Br)-2PACz were 1.38 ns and 1.77 ns, whereas Br-2PACz had 2.47 ns. The high degree of interfacial recombination for 2PACz impacted the hole extraction rates, leaving it as an outlier. Further details of the fitting parameters for the PB kinetics and t_{diff} are provided in the supplemental information (Tables S4–S6; Note S2).

Please cite this article in press as: Torres Merino et al., Impact of the valence band energy alignment at the hole-collecting interface on the photostability of wide band-gap perovskite solar cells, Joule (2024), https://doi.org/10.1016/j.joule.2024.06.017

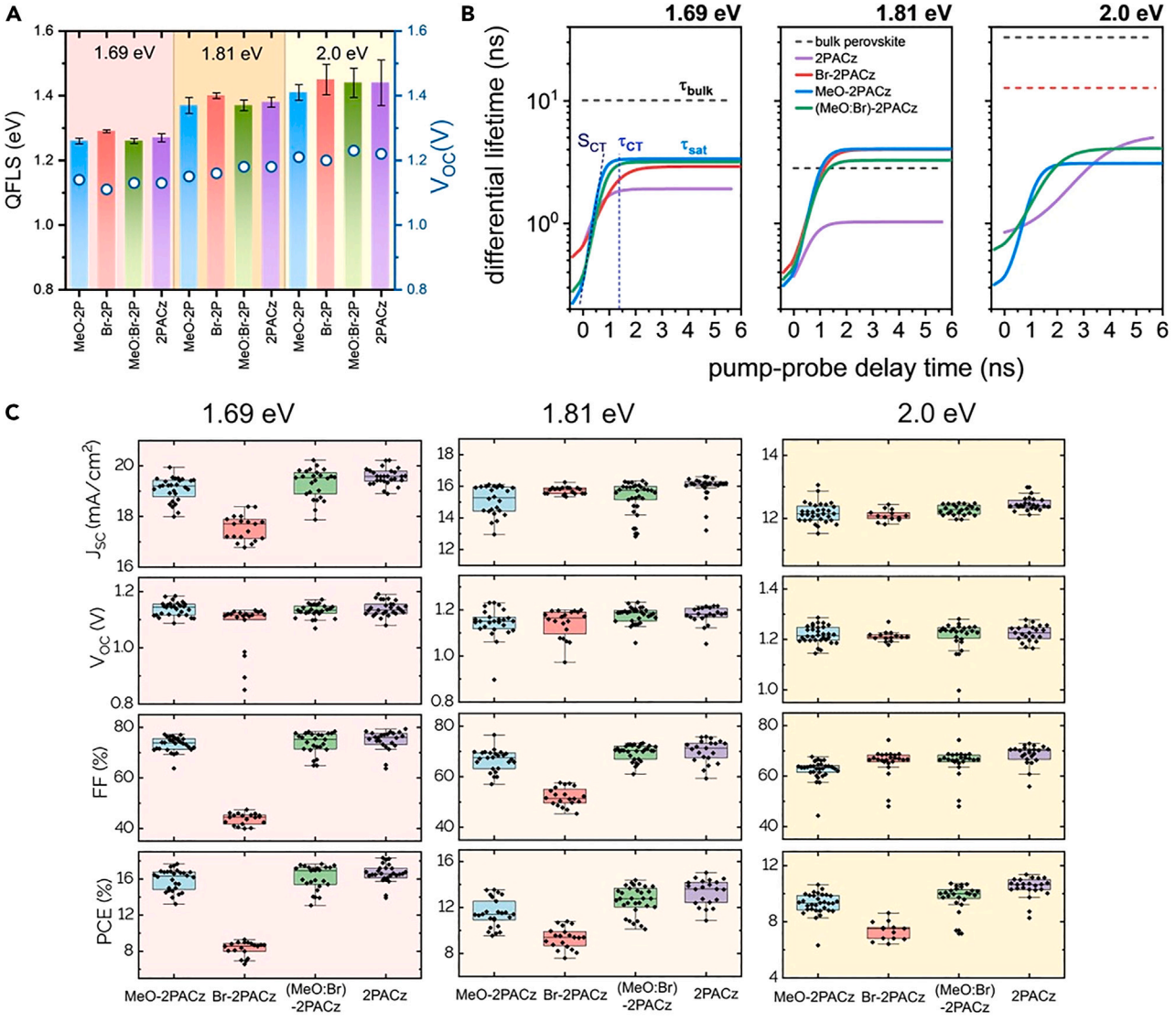

Figure 2. Performance of SAM/perovskite interface

(A) Quasi-fermi level splitting (QFLS) (glass/ITO/HTL/perovskite) and median V_{OC} for each perovskite band-gap PSC (1.69, 1.81, and 2.00 eV) with different SAM HTLs (MeO-2PACz, Br-2PACz, MeO:Br-2PACz mixture, and 2PACz). Error bars correspond to the standard deviation of each QFLS calculated value.

(B) Differential lifetimes (t_{diff}) of the three different perovskites on different ITO/SAM interfaces. The differential lifetimes were calculated from biexponential fits to the normalized TA photobleach signals ($\Delta T/T_n$), using the equation: $t_{diff} = -\{d\ln(\Delta T/T_n)/dT\}^{-1}$. The dashed lines represent monoexponential decay fits to the bulk perovskites/quartz (black; t_{bulk}) or to the Br-2PACz/2.0 eV perovskite sample (red). The slope of the charge transfer decay (S_{CT}), the time corresponding to the completion of charge transfer (t_{CT}), and the saturation lifetime (t_{sat}) are all shown for the example of MeO-2PACz/1.69 eV perovskite.

(C) Spin-coated WBG SJ PSC performance statistics from J-V curves for each perovskite band gap and SAM-HTL combination. Active area: 0.1 cm^2.

Device performance and photostability

Figure 2C shows that for all three perovskite band gaps, Br-2PACz devices underperform compared with the other three HTLs. To quantify the PSC performance losses for distinct HTLs, we made use of the median values (fill factor [FF], open-circuit voltage [V_{OC}], and short circuit current density [J_{SC}]) obtained with device statistics (Figure 2C; Tables S7–S10). When using Br-2PACz as the HTL with the three band gaps, a significant performance loss originates from the FF (~absolute 20%–30%

Please cite this article in press as: Torres Merino et al., Impact of the valence band energy alignment at the hole-collecting interface on the photostability of wide band-gap perovskite solar cells, Joule (2024), https://doi.org/10.1016/j.joule.2024.06.017

less than the PSCs with the other SAM HTLs). The main effect of a barrier (of such magnitude as the one given by Br-2PACz in any of the here presented perovskites) is to lower the FF, but there is a slight loss in J_{SC} and V_{OC} observed as well (Tables S7 and S8). A V_{OC} loss is typically caused by an offset—which can be seen for MeO-2PACz, especially for 1.81 eV and 2.0 eV perovskites—rather than a barrier.[19] Moreover, relative to V_{OC} losses, as shown in Figure 2A, the larger differences between QFLS and V_{OC} were obtained with Br-2PACz in any of the three perovskites (Figures 2A and 2C; Table S8). We believe that this could be explained by the presence of a shunt that impacts the V_{OC} more significantly in the presence of a barrier compared with the aligned case as shown in Figure S22. Device shunts can happen due to several reasons—one of them is caused by mobile ions.[49] This will be discussed further in the last section.

By comparing the percentiles of the box plots (Figure 2C), we can assume that there is no significant statistical difference between the performance of MeO-2PACz, 2PACz, and (MeO:Br)-2PACz-based PSCs. Importantly, for 1.69 eV spin-coated WBG SJ PSCs, (MeO:Br)-2PACz achieved the highest median PCE, while 2PACz showed the highest median PCE for 1.81 and 2.00 eV spin-coated WBG SJ PSCs (Table S10). We note that the PCE of the champion WBG PSCs presented in this work (Table S10) lies below ~15% relative to the PCE from previously reported WBG PSCs in highly efficient tandems.[22,37,40] One of the main reasons for this is that bulk passivation boosts the PCE by suppressing non-radiative losses.[6,47] As the aim of this work is to study solely the HTL/perovskite interface without the effect of perovskite passivation,[9] we intentionally kept pristine the perovskite films here presented to observe the possible extended PSC lifetime by purely optimizing the SAM_{VBM}/PVK_{VBM} interface.

The non-encapsulated spin-coated WBG 1-J PSCs were subjected to 20 min of maximum power point (MPP) tracking to understand the photostability of the distinct SAM HTLs (Figure S23). The PSCs with Br-2PACz showed fast degradation within the first 2 min in both voltage and current density, leading to a power loss of ~65% for all three perovskite band gaps. The blended SAM, (MeO:Br)-2PACz, on the other hand, demonstrated a more stabilized power output at the MPP (P_{MPP}) for each of the three perovskite band-gap compositions. To further test their photostability for a longer period and to prevent moisture and oxygen exposure during the measurement, we used a glass-glass encapsulation with butyl rubber as edge sealant on the PSCs, as previously reported by Babics et al.[50] For the long-term stability studies, we excluded the Br-2PACz-based devices as they degraded within 20 min of MPP tracking.

Figure 3A shows continuous MPP-tracked output power obtained for three WBG configurations with MeO-2PACz, (MeO:Br)-2PACz, and 2PACz HTL for 600 h. Figures S24 and S25 illustrate the corresponding V_{MPP} and J_{MPP} evolution to achieve MPP. For 1.69 eV, 2PACz was the least stable, showing fast voltage and current density losses within the first hour. MeO-2PACz-based 1.69 eV PSCs followed with voltage and current density losses after the first 200 h. Similarly, for 1.81 eV PSCs, 2PACz was the least stable, showing rapid voltage and current density losses within the first 10 h. For 1.81 eV PSCs with MeO-2PACz, although the voltage was stable, the rate loss of current density was higher than (MeO:Br)-2PACz. For 2.00 eV PSCs, with (MeO:Br)-2PACz and 2PACz PSCs, the V_{MPP} was relatively stable, and differences arose from J_{MPP} losses. (MeO:Br)-2PACz leads to the lowest rate of J_{MPP} degradation for each of the three perovskite band gaps, corresponding to lower P_{MPP} losses. The spin-coated 1.69 eV SJ PSCs based on (MeO:Br)-2PACz blended SAM retained 80% of the initial PCE after 900 h under continuous illumination at

Please cite this article in press as: Torres Merino et al., Impact of the valence band energy alignment at the hole-collecting interface on the photostability of wide band-gap perovskite solar cells, Joule (2024), https://doi.org/10.1016/j.joule.2024.06.017

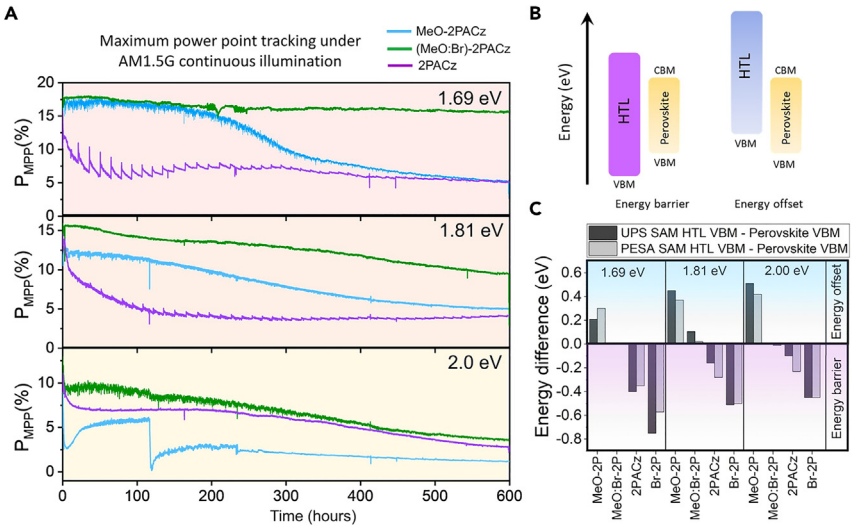

Figure 3. Impact of energy alignment on long-term stability

(A) Continuous MPP tracking of encapsulated devices under AM1.5G (and ~40°C) with the different band-gaps/HTL blend.

(B) Schematic depicting energy barrier and energy offset at the HTL/perovskite interface.

(C) Calculated energy barriers and offsets for each HTL/perovskite blend, magnitudes obtained by UPS and PESA.

AM1.5G (Figure S26). The photostabilities (at T_{80}—which is defined by the time taken to degrade the initial PCE to its 80%) shown in Figures 3A and S26 for the perovskites 1.69 and 1.81 eV reached comparable photostabilities to the WBG subcells used in some highly efficient tandems,[22,37] highlighting the great benefit from solely optimizing the alignment at the SAM_{VBM}/PVK_{VBM} interface. On the other hand, for the wider band-gap perovskite absorber (2.0 eV) with (MeO:Br)-2PACz, the T_{80} was certainly lower than that of the WBG subcell reported in its respective highly efficient tandem,[40] due to the inherent increased speed of phase segregation if no bulk passivation is used in these wider band gaps.[6,40]

One of the reasons for PSC J_{MPP} losses originates from mobile ions within the perovskite layer.[26,51–54] Moreover, as previously mentioned, WBG perovskites show prominent halide segregation into bromide- and I-rich regions, and such segregation limits both performance and stability.[6,11] Furthermore, some SAMs tend to decelerate phase segregation compared with other HTLs due to passivation at the HTL/perovskite interface and energy matching between HTL/perovskite VBMs.[9,22,27,28] To disentangle these effects, we can see that the standalone HTLs, Br-2PACz and MeO-2PACz, yielded less stable device results compared with (MeO:Br)-2PACz. Also, even though 2PACz-based PSCs demonstrate better PCE in a few configurations, they lag behind the blended SAM in photostability; we provide an explanation to this effect in the second last section. Our results show that the energy barriers or offsets at the HTL/perovskite interface (Figures 3B and 3C) can profoundly impact the WBG PSCs' long-term photostability. To further understand the degradation differences in Figure 3A, we tracked the PL evolution of half-stack devices under continuous illumination equivalent to AM1.5G (Figures 4A, 4B, and S27–S30). For this, we analyzed 2PACz and (MeO:Br)-2PACz, representing the energy barrier and the energy-matching cases, respectively. We note that we chose these two SAM HTLs for PL evolution, given the larger differences between high performance and high photostability (Figures 2C and 3A).

Please cite this article in press as: Torres Merino et al., Impact of the valence band energy alignment at the hole-collecting interface on the photostability of wide band-gap perovskite solar cells, Joule (2024), https://doi.org/10.1016/j.joule.2024.06.017

Decelerating phase segregation with (MeO:Br)-2PACz

Figure 4A compares the PL peak evolution of the 1.69 eV perovskite over 40 min of continuous 1 sun (AM1.5G) illumination for both HTLs, 2PACz, and (MeO:Br)-2PACz. For this, we measured the PL signal every minute, leading to 40 scans for each sample. The PL evolution was deconvoluted using Gaussian fitting to obtain two peaks corresponding to the mixed-halide phase and the segregated perovskite phase (I-rich). Figure 4B shows the evolution of the intensity ratio between the different perovskite phases (I-rich/mixed halide) (Figure S27). The I-rich phase evolved rapidly when 2PACz was used as the HTL in contrast to (MeO:Br)-2PACz (Figure 4B). For the 1.81 and 2.0 eV perovskite samples, we observed a significant PL signal coming from intermediate phases (Figure S28); accordingly, we fitted the PL spectra with three Gaussian peaks, which correspond to the emission from the mixed-halide phase, intermediate phase, and I-rich phase. Therefore, in addition to the I-rich/mixed-halide PL intensity ratio, we also tracked the intermediate phase's peak position as a function of time (Figures S29 and S30). Interestingly, for the 1.81 eV perovskite with 2PACz, an exponential decay of the intermediate phase over time was observed, suggesting prominent accelerated segregation in contrast to the linear behavior observed with (MeO:Br)-2PACz (Figure S29B). For the 2.0 eV perovskite, we observed an exponential decay of the intermediate phase for the two HTLs. Nevertheless, 2PACz shows a more pronounced decay when compared with (MeO:Br)-2PACz. Furthermore, when tracking the intensity of the I-rich phase as a function of time (Figures S29C and S30C), 2PACz showed an accelerated increase compared with (MeO:Br)-2PACz for 1.81 and 2.0 eV perovskite layers. This analysis suggests that the segregation dynamics of (MeO:Br)-2PACz are slower compared with 2PACz for the three perovskite band gaps. However, for the 2.00 eV perovskite samples, the differences in the segregation dynamics between 2PACz and (MeO:Br)-2PACz were less, likely due to a much stronger inherent tendency of the perovskite to segregate in agreement with previous reports.[6,40] Furthermore, while typically only two emitting phases are considered in the segregated perovskite, we note that multimodal distributions were observed by PL, in agreement with previous reports.[51,52]

To visualize this phase segregation, we performed cross-section elemental mapping of both 1.69 eV PSCs (2PACz and (MeO:Br)-2PACz as HTLs) after MPP tracking for 40 min by scanning transmission electron microscopy (STEM) (Figures 4C and S31). For 2PACz-based PSCs, an accumulation of iodide was observed at both the HTL and ETL interfaces with an iodide depletion region at the center of the bulk perovskite. However, no obvious iodide accumulation was observed for (MeO:Br)-2PACz-based PSCs (Figure 4C). The elemental mapping observations agree with the PL evolution, indicating prominent phase segregation in 2PACz samples.

To further investigate the carrier transport losses within a larger time interval (nano- to milliseconds) than the one monitored by TA (order of tens of nanoseconds) (Figure S21), we performed Tr-SPV measurements (Figures 4D and S32; Table S11). The measured Tr-SPV responses were then modeled using a minimalistic kinetic model, similar to the one described by Levine et al.[31] For the 1.69 eV perovskite, the hole transfer rate (k_h) is larger with 2PACz ($8 \times 10^5\ s^{-1}$) in comparison with MeO-2PACz ($1.09 \times 10^5\ s^{-1}$), as in agreement with a previous report.[31] It can be seen from Table S11 that when using (MeO:Br)-2PACz ($4 \times 10^5\ s^{-1}$), the hole transfer rate is slightly lower than 2PACz. Nevertheless, we found that the hole-back transfer rate (k_{hb}) is one order of magnitude lower with (MeO:Br)-2PACz ($3.03 \times 10^3\ s^{-1}$) when compared with 2PACz ($9.09 \times 10^4\ s^{-1}$) (Table S11). This indicates significantly lower

Please cite this article in press as: Torres Merino et al., Impact of the valence band energy alignment at the hole-collecting interface on the photostability of wide band-gap perovskite solar cells, Joule (2024), https://doi.org/10.1016/j.joule.2024.06.017

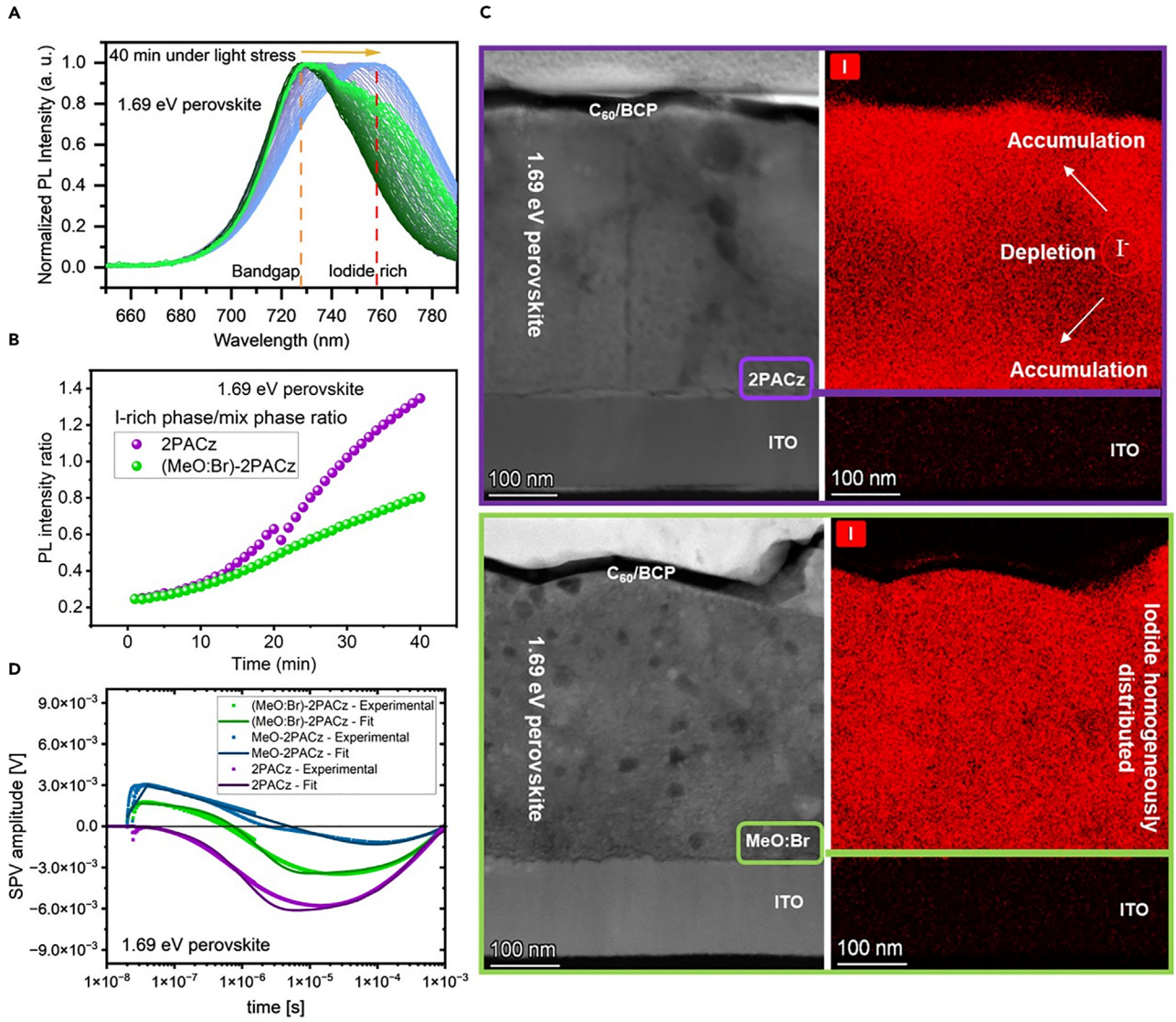

Figure 4. Illumination impact on 1.69 eV perovskites with distinct HTLs

(A) Evolution of PL emission peak of 1.69 eV perovskite tracked over 40 min with 2PACz (blue) and (MeO:Br)-2PACz (green) HTLs.

(B) PL intensity ratio of segregated and mix perovskite phases over 40 min showing faster segregation when 2PACz was used in contrast to (MeO:Br)-2PACz.

(C) Cross-sectional HAADF-STEM image with corresponding elemental mapping (STEM-EDS) of complete device stack after 40 min of MPP tracking under AM1.5G (Figure S18).

(D) Tr-SPV of half-stack devices (ITO/HTL/perovskite).

recombination of de-trapped and back-transferred charge carriers at the HTL/perovskite interface when (MeO:Br)-2PACz was used. Analogously, a similar behavior was observed in 1.81 eV samples (Figure S32; Table S11), but interestingly, we found that MeO-2PACz possesses a positive SPV signal at long times, indicating electron transport toward the ITO, resulting in a poorly selective ITO/HTL interface. We conclude that not only the hole transfer rate (nano- to microseconds) is relevant for photostability but also the hole-back transfer rate (micro- to milliseconds). This is in agreement with a previous work, suggesting that PTAA as HTL leads to an increase of hole-back transfer, resulting in an increase of the I-rich PL emission.[9] Our observations highlight the relevance of disentangling the so-called passivation from of

SAM_{VBM}/PVK_{VBM} interface alignment to significantly reduce the hole-back transfer rate, which in turn will result in decreasing the phase segregation rate.

The role of energy-level matching at the HTL/perovskite interface

To further understand the role of transfer rates in phase segregation, we performed charge carrier density and mobile ion density simulations of devices (at 0.96 and 1 V, respectively) with energy barriers, offsets, and energy-level matching between SAM_{VBM} and PVK_{VBM}. We note that the simulations presented here are based on recently developed device models for triple cation-based PSCs in Diekmann et al.[55,56] using the semiconducting thin film optics simulation software (SETFOS).[57] Figure 5A shows the charge carrier (electron and hole) densities at the HTL/perovskite interface for each configuration: (1) HTL VBM with energy barrier (100 meV), (2) HTL VBM with energy offset (300 meV), and (3) HTL VBM aligned.

In the presence of an offset, the density of holes within the HTL was about one order of magnitude higher than the case when the VBMs were aligned. In the presence of an energy barrier, the density of holes within the perovskite was about two orders of magnitude higher than the density obtained for aligned HTL VBMs. Furthermore, when the VBMs had an offset, the density of electrons was three orders of magnitude higher than the density of holes within the perovskite, which is an inverted behavior when compared with the case of a barrier or VBM aligned, where the density of holes is larger than the density of electrons within the perovskite. If we now consider the mobile ion density distribution across the perovskite film (Figures 5B and 5C), when the VBMs were aligned, the anion density was lower in comparison with the configuration with an energy barrier. Moreover, when the VBMs were offset, the density of anions was higher than the density of cations, showing an inverted behavior compared with the case of a barrier or VBM aligned, where the density of cations was larger than the density of anions. These observations suggest that energy barriers lead to an accumulation of holes within the perovskite near the HTL/perovskite interface, which triggers an accumulation of anions at the interface. At the same time, offsets lead to an accumulation of electrons within the perovskite near the HTL/perovskite interface, triggering an accumulation of cations at the interface. To be able to compare these computational simulations with the experimental results from half-stacks (glass/ITO/SAM/perovskite) characterized by PL evolution and Tr-SPV, we further calculated the charge carrier and mobile ion density distributions at open-circuit conditions obtaining a similar behavior as the one discussed above (held at 1 V) (Figure S33). We remark that the trends observed in Figures 5A–5C and S33 will depend on the magnitude of the formed offsets or barriers, which can become more prominent if their magnitude increase leading to greater differences on photostabilities as the ones displayed in Figure 5D. This is in agreement with our results shown in Figure S23 where the magnitude of the barrier formed with Br-2PACz is much higher than that of 2PACz for any of the three spin-coated perovskite band gaps studied in this work (Figure 3C).

Mechanism

We propose the following working mechanism to explain systematically how SAM_{VBM}/PVK_{VBM} energy alignment, charge transport, phase segregation, and long-term photostability correlate through an interface-altered electric field in contrast to other known pathways for induced phase segregation in WBG perovskites.[17,20,43–45,58] For this, it is first important to analyze in detail compositional differences with growth surfaces on distinct SAMs, as we did observe differences in crystal properties in Figure S16. We added a thorough analysis in the supplemental information through GIWAXS (Note S3; Figures S34–S43; Tables S12 and S13) for

Please cite this article in press as: Torres Merino et al., Impact of the valence band energy alignment at the hole-collecting interface on the photostability of wide band-gap perovskite solar cells, Joule (2024), https://doi.org/10.1016/j.joule.2024.06.017

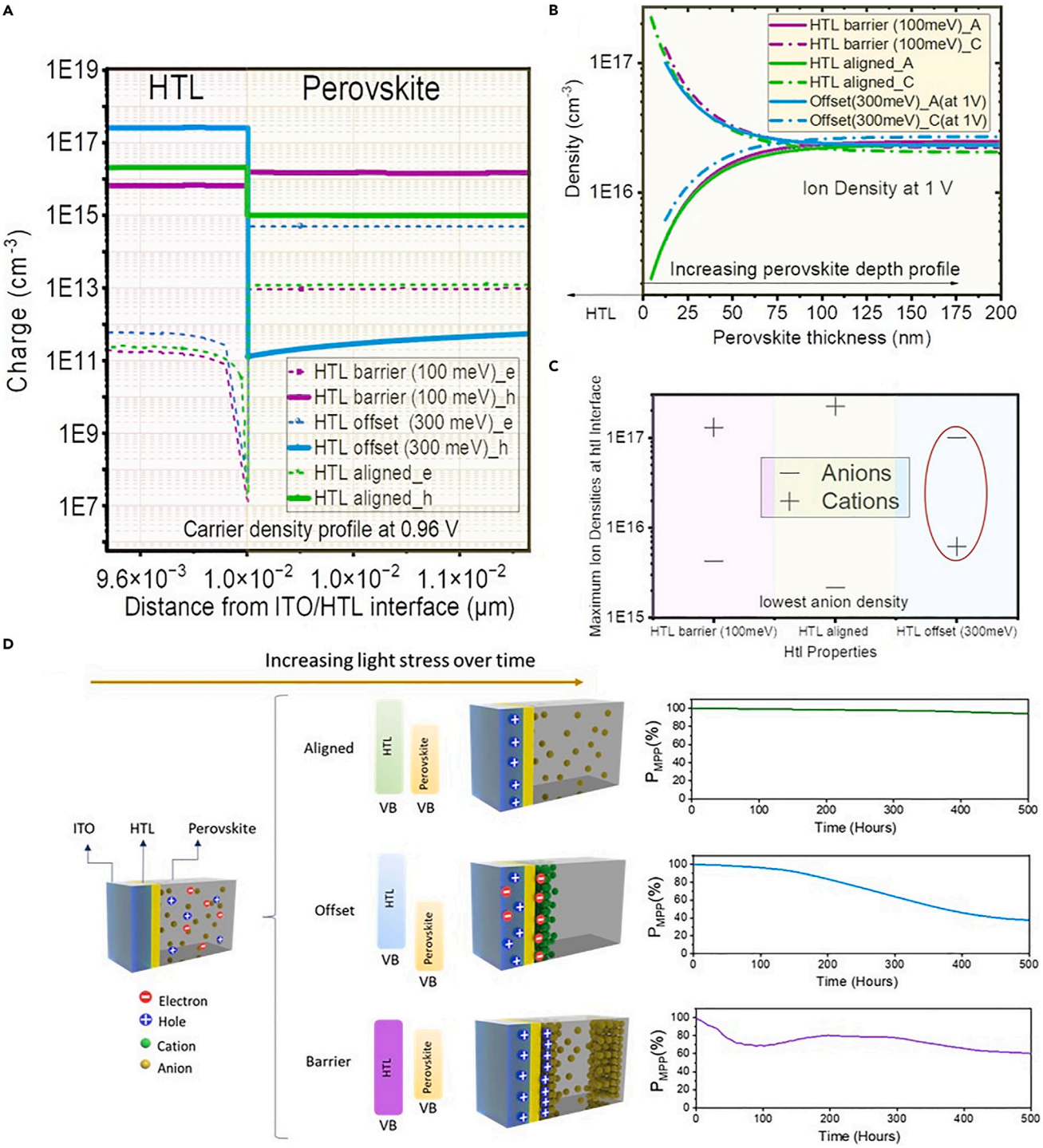

Figure 5. The role of VBM matching at HTL/perovskite interface on long-term photostability

(A–C) Computational simulations of valence band energy offset, alignment, and barrier between the HTL and the perovskite layer of (A) charge carrier (electrons [e] and holes [h]) density distribution at the HTL/perovskite interface at 0.96 V. (B) Mobile ion (cations [C] and anions [A]) density distribution across the perovskite film adjacent to the HTL/perovskite interface at 1 V. (C) maximum mobile ion densities at the HTL/perovskite interface at 1 V. (D) Minimalistic scheme of charge density and mobile ions under light stress at the HTL/perovskite interface when their VBMs are aligned, in offset or in barrier, and smoothed normalized MPPT of 1.69 eV devices under AM1.5G.

Please cite this article in press as: Torres Merino et al., Impact of the valence band energy alignment at the hole-collecting interface on the photostability of wide band-gap perovskite solar cells, Joule (2024), https://doi.org/10.1016/j.joule.2024.06.017

which we are certain that we do not observe correlations between crystallinity/texture/secondary phases/halogen interface formation and spectroscopy/performance/photostability for any of the three spin-coated perovskite band gaps when using the four distinct SAMs (MeO-2PACz, 2PACz, Br-2PACz, and (MeO:Br)-2PACz). Yet we observe clear correlations between energy-level alignment at the HTL/perovskite interface and photostability of the studied SAM/perovskite combinations. Such clear correlation was further tested in a completely different perovskite composition by a different deposition method "hybrid," obtaining the expected result where VBM alignment led to improved photostability (Note S4; Figures S44 and S45); details are provided in the supplemental information. Having said that, we can now focus solely on the link between SAM_{VBM}/PVK_{VBM} alignment and long-term photostability.

In PSCs, the charges (both free carriers and mobile ions), in general, are drawn toward their respective electrodes, that is, holes and cations toward the cathode and electrons and anions toward the anode. However, in the presence of a SAM_{VBM}/PVK_{VBM} barrier, holes tend to accumulate within the perovskite at the HTL/perovskite interface (Figures 5A and 5D). This leads to an electric field that pulls more anions toward the HTL interface than is the case with aligned VBMs (Figures 5B–5D). According to our observations, these anions (predominantly iodides, as characterized by transmission electron microscopy [TEM] [Figure 4C]), in agreement with other reports, act as low-energy-gap charge carrier funneling regions within the perovskite layer (Figures 4A and 4B).[6,8,9] Our TEM analysis reveals that iodide accumulation is present at both HTL/perovskite and perovskite/ETL perovskite interfaces (Figure 4C). To understand the accumulation of ions on both interfaces, we added a note in the supplemental information including experimental evidence of the influence of the altered electric field at the SAM_{VBM}/PVK_{VBM} interface on ion accumulation at the perovskite/ETL interface (Note S5). Moreover, a (weakened) electric field is produced from such accumulation of ions, minimizing charge extraction at the interface (Note S6).[53,54,59] Analogously, in the presence of an offset, a significant density of electrons is accumulated within the perovskite layer at the HTL/perovskite interface, drawing cations to this interface (Figure 5). This is corroborated by the inverted experimental Tr-SPV and SPV and simulated SPV signals observed for an offset (MeO-2PACz) in 1.81 eV perovskite samples (Figures S32, S46, and S47), and it is further characterized by STEM-energy dispersive spectroscopy (EDS), confirming the presence of cations (cesium) at the interface (Figure S48). It is important to highlight that both iodide (anions) and cesium (cations) were observed in the presence of SAM_{VBM}/PVK_{VBM} barrier and SAM_{VBM}/PVK_{VBM} offset (Figures 4C, S48, and S49). This can be explained by the offset formed between the CBMs at the perovskite/ETL interface (Figure S3 and being the CBM of the C60 as the one we previously reported[60]). We have added a note on these latter observations to the supplemental information (Note S7), highlighting the importance of interface alignment at both ETL and HTL interfaces.[21]

Therefore, with well-aligned VBM levels at the HTL/perovskite interface, such accumulation of ions is reduced, leading to minimized halide segregation as with the (MeO:Br)-2PACz-based HTL, enhancing the long-term photostability of WBG PSCs (Figures 3A and S52).

DISCUSSION

By reducing the energetic VBM mismatch between the HTL and perovskite absorber, we observed minimized halide segregation when the SAM blend (MeO:Br)-2PACz

Please cite this article in press as: Torres Merino et al., Impact of the valence band energy alignment at the hole-collecting interface on the photostability of wide band-gap perovskite solar cells, Joule (2024), https://doi.org/10.1016/j.joule.2024.06.017

was used. From the observed carrier transport characterizations, we highlight some of the most important observations: (1) Tr-SPV provides insights into the energy loss processes influencing the PSC performance by determining hole extraction and hole-back transfer rates. Additionally, we observed an anticorrelation between hole-back transfer rates and PSC photostability. (2) When tracking the PL evolution of half-stack devices over time under continuous AM1.5G-equivalent illumination, we can predict which interface is less prone to promote halide segregation. (3) Elemental mapping by STEM-EDS reveals that such ion accumulation—originating from halide segregation—occurs at both HTL and ETL perovskite interfaces. (4) Computational simulations of the mobile ion distribution suggest that in the presence of charge carrier accumulation at the HTL—arising from an energy barrier or offset between SAM_{VBM} and PVK_{VBM}—ion accumulation is triggered, which we attribute to the altered electric field developed at the HTL/perovskite interface. We propose energy matching at the HTL/perovskite interface to increase the device performance and, most importantly, to enhance the device photostability in WBG PSCs. In fact, when (MeO:Br)-2PACz was used in encapsulated WBG SJ PSCs, it was possible to retain up to 80% of the initial PCE when held at the MPP under continuous AM1.5G-equivalent conditions up to 900, 378, and 60 h for 1.69, 1.81, and 2.0 eV double cation, non-passivated perovskites, respectively.

EXPERIMENTAL PROCEDURES

Resource availability

Lead contact

Further information and requests for resources should be directed to and will be fulfilled by the lead contact, Stefaan De Wolf (stefaan.dewolf@kaust.edu.sa).

Materials availability

This study did not generate new, unique materials.

Data and code availability

The datasets generated during this study are available from the lead contact upon reasonable request.

Fabrication of perovskite solar cells

Materials

The 15 ohms/sq pattern ITO glass was obtained from Xinyan Technology. SAM molecules: MeO-2PACz and 2PACz were obtained from TCI, and Me-4PACz, Br-2PACz, and 2PACz were obtained from Lumtec. Anhydrous 98.99% ethanol was purchased from VWR. Ag pellets were obtained from Kurt J. Lesker Company. Precursors for perovskite: FAI from greatsolar; PbI_2 and $PbBr_2$ anhydrous beads from Sigma Aldrich; and CsI powder from Sigma Aldrich. Dimethyl sulfoxide, dimethylformamide, and chlorobenzene from Sigma Aldrich. C_{60} powder from nano-C and bathocuproine 99.99% from Sigma Aldrich. MgF_2 was purchased from Plasmaterials.

Methods

Spin-coated perovskites. The perovskite solution was prepared by mixing $PbBr_2$, PbI_2, CsI, and FAI in 4:3 DMF:DMSO at 1.1 M with stoichiometry given by $FA_{0.83}Cs_{0.17}Pb(Br_XI_{1-X})_3$ and stirred overnight. We note that by varying X = 0.3, 0.5, and 0.7, we obtained the band gaps 1.69, 1.81, and 2.00 eV, respectively. All SAM solutions were prepared at a concentration of 1 mM in anhydrous ethanol and ultrasonication for 15 min. ITO substrates were cleaned by using ultrasonic bath with detergent water, deionized water, acetone, and isopropyl alcohol (IPA) sequentially for 15 min, and the residue solvent was dried by clean air blowing,

followed by UV ozone treatment for 15 min. After ozone treatment substrates were transferred inside the glovebox at <0.1 ppm of H_2O and O_2 under constant purging. The SAM solutions were spin coated at 3,000 rpm for 30 s and then annealed at 100°C for 10 min. Alternatively, rinsing SAM films was done by dropping 3 times 200 μL anhydrous ethanol on intervals of 15 s during dynamic spinning at 5,000 rpm for 45 s. After this, the perovskite ink was spin coated at 4,000 rpm for 30 s. After the first 20 s, 80 μL of antisolvent (chlorobenzene) was dropped. Substrates were then annealed for 25 min at 100°C. The substrates were kept under nitrogen atmosphere and transferred to the evaporator where a C_{60} film of 10 nm was deposited at a rate of 0.1 Å/s. Subsequently, 5 nm of bathocuproine was sublimed at a rate of 0.1 Å/s. Then 100 nm of Ag was deposited at a rate of 0.2 Å/s for the first 10 nm and 3 Å/s for the rest 90 nm. A 100 nm MgF_2 layer is employed as an antireflective layer on the glass side to minimize reflection losses.

Hybrid perovskites. The ITO preparation was the same as the one explained above for the spin-coated perovskite single junction devices. Alternatively, Me-4PACz and (MeO:Br)-2PACz in 20:80 ratio were employed as HTLs processed in the same manner as the one described above for spin-coated perovskite single junction devices. The deposition of 1.68 eV hybrid processed-perovskite started with the evaporation of 220 nm PbI_2:CsBr with a ratio of 1.0:0.1 A/s, respectively. The perovskite layer was obtained by spin coating FAI/FAB/MACl in ethanol at 4,000 rpm. The final conversion occurred after annealing the substrates at 150°C for 30 min in a controlled humidity chamber. Single junction devices were finalized with C60/BCP/Ag as described in the methodology for spin-coated perovskite single junction devices.

Instruments and measurements

Simulated AM1.5G illumination tests

The J-V curves of the above devices were obtained from a Keithley 2400 source meter under simulated AM 1.5G illumination via Sun 3000 solar simulator from Abet Technologies. For calibrating the spectral emission, a KG-5 filter-covered mono-silicon standard cell from Newport was used. The scan speed was 200 mV/s with a dwell of 0.01 V. The J-V measurements were performed with an aperture area of 0.1 cm^2 and under ambient temperature within a nitrogen glovebox. The same setup was employed to track the operational stability of unencapsulated devices under AM1.5G and at ~40°C. The long-term operational stability tests for encapsulated devices were carried out with a Solixon A-70-CU-2, equipped with mixed-gas plasma bulbs. MPPT measurements were performed using Automatic Research trackers, which have a resolution of <10 μV/100 nA, following a three-point perturbation method. The MPP was tracked under AM1.5G illumination in ambient air at ~40°C. The voltage at the MPPT was automatically applied, and the power output of the devices was tracked.

PESA

PSEA measurements were conducted in a Hitachi, Riken AC-2 system with a UV source. The valence band maximum was calculated from the linear fit of the photoemission signal originated from the sample respect to the ground signal.

UPS and IPES

The electron spectroscopy measurements of UPS and low-energy inverse photoemission spectroscopy (LE-IPES) were conducted in a single UHV ScientaOmicron system at 10^{-9} mbar.

Please cite this article in press as: Torres Merino et al., Impact of the valence band energy alignment at the hole-collecting interface on the photostability of wide band-gap perovskite solar cells, Joule (2024), https://doi.org/10.1016/j.joule.2024.06.017

The surface WF and VBM were studied by UPS with a vacuum ultraviolet unfiltered He(1) (21.22 eV) source (focus). The samples were biased by 10 eV to observe the secondary electron cutoff. The photoelectrons were collected at an angle of 80° between the sample and analyzer, with a normal electron take-off angle. The constant analyzer pass energy (CAE) was 5 eV for the valence band region and for the secondary electron cutoff.

The surface CBM was studied by IPES, which was conducted in a home-built chamber consisting of an electron source (Staib) operating at 20–30 eV with an energy dispersion of 0.25 eV directed normally to the sample. The sample was biased to 20 eV. All extraneous light was eliminated during measurements by covering port windows and sealing the detector. Plots of UPS and IPES are constructed considering the shared EF position and arbitrarily adjusted in intensity.

FIB- and TEM-based measurements

Microstructural and elemental mapping studies of the device along cross-section were performed by STEM. For TEM electron transparent (~75 nm) lamella was prepared in a scanning electron microscope (SEM Helios G4 DualBeam, FEI), equipped with an EasyLift nanomanipulator and Ga-focused ion beam (FIB). Two types of protective coatings were deposited to protect the region of interest during FIB. First e-beam Pt coating of 0.5 μm, and additional 3 μm ion beam Pt coating for final protection. The ion beam milling procedure was carried out by step-by-step cutting and thinning down lamella to ~75 nm while decreasing beam current (30 kV, 1.2 nA–90 pA) to avoid ion beam damage. Final cleaning was done at a low current (5–2 kV, 81–28 pA) to remove contamination. TEM-based experiments were performed in converge beam STEM mode with high-angle annular dark-field STEM (HAADF-STEM) detection, which is equipped with EDS (STEM-EDS) in Prob Cs-corrected Thermofisher Titan 60-300 Cubed TEM microscope with 300 kV acceleration voltage. A dedicated TEM specimen holder with EI Super-X EDS four-quadrant detector was used to improve elemental mapping. Gatan Digital Micrograph and Thermo Scientific Velox suites were used to process the datasets.

KPFM

Measurements were done under air atmosphere with an AFM Dimension Icon from Bruker using a SCM-PIT v2 tip, which was coated with reflective platinum-iridium (PtIr) and was based on an RFESP-75 AFM probe. The tip was made of antimony-doped silicon, with a resistivity varying from 0.01 to 0.025 cm. The AFM tip was rectangular in shape with nominal frequencies and stiffness values of 75 KHz and 4 Nm^{-1}. KPFM measurements were done by implementing Lift Mode surface potential imaging, so-called amplitude modulated KPFM (AM-KPFM), where surface topography is obtained by standard TappingMode AFM in the first pass and the surface potential is measured in the second pass. The reference sample was a highly ordered pyrolytic graphite (HOPG) freshly cleaved. Before and after each measurement the tip was calibrated. WF values are determined as an average of a minimum of three independent scans, which were obtained by scanning a minimum of three different areas of the sample. 15 ohms/sq ITO glass obtained from Xinyan Technology were used as substrates. The sample preparation was the same as the one described for device fabrication.

QFLS calculation

The measurements were conducted using the IMA hyperspectral microscope from photon, etc. Photoluminescence signals were collected from the active area of 440 μm × 320 μm. A 405 nm continuous wave laser was used as an excitation source

with the output power close to 1 sun condition. To increase the signal-to-noise ratio, the exposure time for each wavelength was set to 1 s. The collected data was analyzed using a home-built MATLAB code. The calculation of the quasi-fermi level splitting was based on the generalized Planck's law. The statistical distributions (Figure 1) show the calculated QFLS from the active area, with each single count value representing the QFLS of a 3 μm × 3 μm pixel. The theoretical model that we used for this method can be found in Aydin et al.[61]

DFT computational details

The geometries of the SAMs are optimized in the gas phase using Gaussian09[62] with the B3LYP functional at the 6-311G(d,p) level of DFT. The obtained dipole moments are given in Figure 1D. They depend on the head group and agree well with earlier reports.[27,28,30] A higher dipole moment increases the ionization energy of the SAM. The corresponding electrostatic potential maps are shown in Figure S11.

Tracking PL evolution

Measurements were performed on the half-cell layer stacks. Samples were illuminated from the PVK side with a 405 nm continuous wave laser (Cobolt MLD-06) for 20 min for both 1.81 and 2 eV samples and 40 min for 1.69 eV samples. To match the standardized test conditions, the photon dose equivalent to the 1-sun condition was calculated from the AM 1.5G spectrum for respective values of the absorber's band-gap energy; it was then recalculated into the equivalent optical power of the beam incident onto the sample.[63] Emission from the sample was coupled into the spectrometer and recorded with time intervals of 1 min. To isolate the sample from atmospheric effects, the whole setup was placed in the nitrogen-filled glovebox.

Every collected image was normalized to its maximum value. It was then recalculated from wavelength into energy space using Jacobian transformation[64] and subsequently fitted using multiple Gaussian distributions. This allowed us to deconvolute contributions from different emitting perovskite phases (namely, mixed, intermediate, and segregated—I-rich—phases) to the overall signal.

For intensity tracking, the signal at corresponding band-gap energy was taken for the mixed phase, while the value at 1.615 eV was taken for the I-rich phase. This value was selected because the segregated phase emission peak was centered around this value for all three band gaps. The peak position of the intermediate phase was used as a parameter to track the rate of its spectral shift. Recorded values were then plotted versus time to visualize segregation dynamics (Figures 4B, S28, S30, and S31).

Tr-PL measurement and analysis

Samples (glass/ITO/HTL/perovskite) were mounted in the nitrogen-filled chamber while both excitation and emission were coupled through the calcium fluoride viewing port. A Picolo AOT 50-MOPA system was used to create a 532 nm excitation beam with a repetition rate of 50 kHz and fluence of ~500 nJ/cm^2. Emission was focused onto the entrance slit of the spectrometer and subsequently detected with the streak camera unit from Hamamatsu. Obtained 3D images (time, wavelength, and emission intensity) were then deconvoluted into respective 2D components (spectral and temporal), and the latter was fitted with a double exponential function to obtain "slow" and "fast" lifetime components. An amplitude-averaged lifetime was then calculated by weighing two components with their respective amplitude prefactors and used as a figure-of-merit to compare extraction dynamics in different HTL/perovskite layer stacks.

Please cite this article in press as: Torres Merino et al., Impact of the valence band energy alignment at the hole-collecting interface on the photostability of wide band-gap perovskite solar cells, Joule (2024), https://doi.org/10.1016/j.joule.2024.06.017

Tr-SPV

The Tr-SPV setup measures the (surface) voltage that builds up between the front surface and back electrode after the photogeneration of charge carriers in the absorber layer and the subsequential separation of electrons and holes.[65] To this end, a fixed capacitor arrangement is used, in which the back electrode (ITO) is contacted. At the front side, an insulating cover glass, a fluorine doped tin oxide (FTO), and a high-impedance buffer are placed. The voltage between both electrodes is recorded as a function of time by an oscilloscope (4 GHz). For the photogeneration of a pulsed laser with a wavelength of 515 nm, pulse width of ~150 fs, a repetition rate of 125 kHz, and a photon flux of 2×10^{15} photons/cm^2/pulse is used. The acquired SPV transients are modeled by a minimalistic kinetic model, which yields charge extraction and recombination lifetimes, trap densities in bulk, and interfaces as was described previously in Levine et al.[31].

TA spectroscopy

TA spectroscopy was carried out using a home-built pump-probe setup. Part of the output of a Ti:sapphire amplifier (Coherent LEGEND DUO, 800 nm, 4.5 mJ, 3 kHz, 100 fs) was split into two beams (2 mJ, 1 mJ). Each of the beams was used to separately pump two optical parametric amplifiers (OPAs; light conversion TOPAS Prime). The 2 mJ TOPAS generated wavelength-tunable pump pulses (240–2,600 nm, using Light Conversion NIRUVIS extension), while the 1 mJ TOPAS generated signal and idler only (1,160–2,600 nm). The pump wavelength was fixed at 532 nm, with a fluence of 500 nJ/cm^2. The output of the 1 mJ TOPAS was fixed to 1,300 nm, which was used as the seed for white light generation by focusing a portion of it through a continuously moving CaF_2 crystal, thereby generating a white light supercontinuum from 350 to 1,100 nm. The pump-probe delay time was achieved by varying the pump path length using a broadband retroreflector mounted on a 600 mm automated mechanical delay stage (Newport linear stage IMS600CCHA controlled by a Newport XPS motion controller), generating delays from −400 ps to 7 ns.

Pump and probe beams were focused on the sample to diameters of 0.49 and 0.06 mm (from a Gaussian fit at 86.5% intensity), as measured using a beam profiler (Coherent LaserCam-HR II). The samples were kept under a dynamic vacuum of $<10^{-5}$ mbar, and pump and probe beams were incident on the substrate side of the sample (i.e., closer to the HTL/perovskite interface). The transmitted fraction of the white light was guided to a custom-made prism spectrograph (Entwicklungsbüro Stresing), where it was dispersed by a prism onto a 512-pixel N-type metal oxide semiconductor linear image sensor (Hamamatsu S8381-512Q). The probe pulse repetition rate was 3 kHz, while the pump pulses were mechanically chopped to 1.5 kHz, and the detector array was read out at 3 kHz. Adjacent diode readings corresponding to the transmission of the sample after excitation and in the absence of an excitation pulse were used to calculate ΔT/T. Measurements were averaged over several thousand shots to obtain a good signal-to-noise ratio. The chirp induced by the transmissive optics was corrected with a home-built MATLAB code.

Photobleach kinetics were monitored by averaging the kinetic traces at the peak wavelength ±~15 nm. The kinetics were fit with a biexponential decay equation: $\Delta T/T = A_0 + A_1 e^{((-t/\tau_1))} + A_2 e^{((-t/\tau_2))}$, where t is the pump-probe delay time, A_i are the amplitudes of the decay components, and τ_i are the lifetimes of the decay components. The quenching efficiency was calculated by comparing the amplitude-averaged lifetime of the perovskite/HTL interface ($t_{ave}^{PVK/SAM}$) to that of the neat perovskite (τ_{ave}^{PVK}), using the equation: $QE = 1 - \frac{t_{ave}^{PVK-SAM}}{t_{ave}^{PVK}}$.

GIWAXS

GIWAXS was carried out using a Xenocs Xeuss 3.0 equipped with a Genix 3D Cu source with focused beam collimation, λ = 1.54 Å, and an Eiger 2R 4M detector. The sample-to-detector distance was 110 mm, and the incidence angle was optimized at 0.6° to probe the film's surface. Each frame was acquired using an exposure of 30 s. Wedge correction and linecut integration were performed using XSACT by Xenocs.

SUPPLEMENTAL INFORMATION

Supplemental information can be found online at https://doi.org/10.1016/j.joule.2024.06.017.

ACKNOWLEDGMENTS

This publication is based upon work supported by the King Abdullah University of Science and Technology (KAUST) Office of Sponsored Research (OSR) under award nos. OSR-CARF/CCF-3079, OSR-2019-CRG8-4093, and OSR-2020-CRG9-4350. C.E.P. acknowledges a KAUST Global Fellowship for Postdocs under award no. ORA-2022-5002. M.S. further acknowledges the Heisenberg program from the Deutsche Forschungsgemeinschaft (DFG, German Research Foundation) for funding project no. 498155101 as well as project nos. 423749265 and 424709669 - SPP 2196 (SURPRISE-2 and HIPSTER-PRO). I. L. thanks the AiF project (ZIM-KK5085302DF0) for financial support.

AUTHOR CONTRIBUTIONS

L.V.T.M. conceived the idea, designed and directed the experimental plan, and performed perovskite PV fabrication and characterization; C.E.P. and O.M. performed TA and PL characterizations guided by F.L.; A.S.S. provided help with perovskite characterization and figure schematics; C.V.F. performed TA characterizations with first insights on halide segregation guided by F.L.; P.D. performed UPS and IPES measurements; B.V. performed FIB and TEM-based characterizations; S.K. and D.R.V. performed GIWAXS characterizations with input from S.D.W. and D.B.; V.H. and E.U. performed PL characterizations for QFLS calculations; S.S. performed PL characterizations of PSCs guided by M.S.; S.S. and N.K. performed charge carrier and mobile ion density simulations guided by M.S.; O.K., H.H. and I.L. performed Tr-SPV characterizations; R.R.P. performed DFT calculations guided by U.S.; S.K. and A.P. performed KPFM characterizations with input from M.M.M.; M.B. encapsulated PV devices; B.Y. and E.A. performed MPP tracking of encapsulated PSCs; A.A.S. fabricated hybrid perovskite PV; S.M., A.R.P., W.R., A.R., and H.A.N. provided help in PV optimization; H.B., T.G.A., and F.H.I. provided scientific validation guided by S.D.W and T.D.A.; L.V.T.M. wrote the manuscript with help from A.S.S., T.D.A., and S.D.W.; S.D.W. supervised the project and secured funding. All authors discussed and revised the manuscript.

DECLARATION OF INTERESTS

The authors declare no competing interests.

Received: November 24, 2023
Revised: March 13, 2024
Accepted: June 19, 2024
Published: July 17, 2024

REFERENCES

1. (2024). Best research cell-efficiency chart. https://www.nrel.gov/pv/cell-efficiency.html.
2. Haegel, N.M., Atwater, H., Barnes, T., Breyer, C., Burrell, A., Chiang, Y.-M., De Wolf, S., Dimmler, B., Feldman, D., Glunz, S., et al. (2019). Terawatt-scale photovoltaics: transform global energy. Science *364*, 836–838. https://doi.org/10.1126/science.aaw1845.
3. Razzaq, A., Allen, T.G., Liu, W., Liu, Z., and De Wolf, S. (2022). Silicon heterojunction solar cells: Techno-economic assessment and opportunities. Joule *6*, 514–542. https://doi.org/10.1016/j.joule.2022.02.009.
4. Eperon, G.E., Hörantner, M.T., and Snaith, H.J. (2017). Metal halide perovskite tandem and multiple-junction photovoltaics. Nat. Rev. Chem. *1*, 0095. https://doi.org/10.1038/s41570-017-0095.
5. Jošt, M., Kegelmann, L., Korte, L., and Albrecht, S. (2020). Monolithic Perovskite Tandem Solar Cells: A Review of the Present Status and Advanced Characterization Methods Toward 30% Efficiency. Adv. Energy Mater. *10*, 1904102. https://doi.org/10.1002/aenm.201904102.
6. Knight, A.J., and Herz, L.M. (2020). Preventing phase segregation in mixed-halide perovskites: a perspective. Energy Environ. Sci. *13*, 2024–2046. https://doi.org/10.1039/D0EE00788A.
7. Ghasemi, M., Guo, B., Darabi, K., Wang, T., Wang, K., Huang, C.-W., Lefler, B.M., Taussig, L., Chauhan, M., Baucom, G., et al. (2023). A multiscale ion diffusion framework sheds light on the diffusion–stability–hysteresis nexus in metal halide perovskites. Nat. Mater. *22*, 329–337. https://doi.org/10.1038/s41563-023-01488-2.
8. Knight, A.J., Borchert, J., Oliver, R.D.J., Patel, J.B., Radaelli, P.G., Snaith, H.J., Johnston, M.B., and Herz, L.M. (2021). Halide Segregation in Mixed-Halide Perovskites: Influence of A-Site Cations. ACS Energy Lett. *6*, 799–808. https://doi.org/10.1021/acsenergylett.0c02475.
9. Lim, V.J.-Y., Knight, A.J., Oliver, R.D.J., Snaith, H.J., Johnston, M.B., and Herz, L.M. (2022). Impact of Hole-Transport Layer and Interface Passivation on Halide Segregation in Mixed-Halide Perovskites. Adv. Funct. Mater. *32*, 2204825. https://doi.org/10.1002/adfm.202204825.
10. Caprioglio, P., Caicedo-Dávila, S., Yang, T.C.-J., Wolff, C.M., Peña-Camargo, F., Fiala, P., Rech, B., Ballif, C., Abou-Ras, D., Stolterfoht, M., et al. (2021). Nano-emitting Heterostructures Violate Optical Reciprocity and Enable Efficient Photoluminescence in Halide-Segregated Methylammonium-Free Wide Bandgap Perovskites. ACS Energy Lett. *6*, 419–428. https://doi.org/10.1021/acsenergylett.0c02270.
11. Kuno, M., and Brennan, M.C. (2020). What Exactly Causes Light-Induced Halide Segregation in Mixed-Halide Perovskites? Matter *2*, 21–23. https://doi.org/10.1016/j.matt.2019.12.004.
12. Motti, S.G., Patel, J.B., Oliver, R.D.J., Snaith, H.J., Johnston, M.B., and Herz, L.M. (2021). Phase segregation in mixed-halide perovskites affects charge-carrier dynamics while preserving mobility. Nat. Commun. *12*, 6955. https://doi.org/10.1038/s41467-021-26930-4.
13. Choe, H., Jeon, D., Lee, S.J., and Cho, J. (2021). Mixed or Segregated: Toward Efficient and Stable Mixed Halide Perovskite-Based Devices. ACS Omega *6*, 24304–24315. https://doi.org/10.1021/acsomega.1c03714.
14. Herz, L.M. (2017). Charge-Carrier Mobilities in Metal Halide Perovskites: Fundamental Mechanisms and Limits. ACS Energy Lett. *2*, 1539–1548. https://doi.org/10.1021/acsenergylett.7b00276.
15. Jiang, Q., Tong, J., Scheidt, R.A., Wang, X., Louks, A.E., Xian, Y., Tirawat, R., Palmstrom, A.F., Hautzinger, M.P., Harvey, S.P., et al. (2022). Compositional texture engineering for highly stable wide-bandgap perovskite solar cells. Science *378*, 1295–1300. https://doi.org/10.1126/science.adf0194.
16. Liu, J., Aydin, E., Yin, J., De Bastiani, M., Isikgor, F.H., Rehman, A.U., Yengel, E., Ugur, E., Harrison, G.T., Wang, M., et al. (2021). 28.2%-efficient, outdoor-stable perovskite/silicon tandem solar cell. Joule *5*, 3169–3186. https://doi.org/10.1016/j.joule.2021.11.003.
17. Barker, A.J., Sadhanala, A., Deschler, F., Gandini, M., Senanayak, S.P., Pearce, P.M., Mosconi, E., Pearson, A.J., Wu, Y., Srimath Kandada, A.R., et al. (2017). Defect-Assisted Photoinduced Halide Segregation in Mixed-Halide Perovskite Thin Films. ACS Energy Lett. *2*, 1416–1424. https://doi.org/10.1021/acsenergylett.7b00282.
18. Stolterfoht, M., Wolff, C.M., Márquez, J.A., Zhang, S., Hages, C.J., Rothhardt, D., Albrecht, S., Burn, P.L., Meredith, P., Unold, T., et al. (2018). Visualization and suppression of interfacial recombination for high-efficiency large-area pin perovskite solar cells. Nat. Energy *3*, 847–854. https://doi.org/10.1038/s41560-018-0219-8.
19. Stolterfoht, M., Caprioglio, P., Wolff, C.M., Márquez, J.A., Nordmann, J., Zhang, S., Rothhardt, D., Hörmann, U., Amir, Y., Redinger, A., et al. (2019). The impact of energy alignment and interfacial recombination on the internal and external open-circuit voltage of perovskite solar cells. Energy Environ. Sci. *12*, 2778–2788. https://doi.org/10.1039/C9EE02020A.
20. Belisle, R.A., Bush, K.A., Bertoluzzi, L., Gold-Parker, A., Toney, M.F., and McGehee, M.D. (2018). Impact of Surfaces on Photoinduced Halide Segregation in Mixed-Halide Perovskites. ACS Energy Lett. *3*, 2694–2700. https://doi.org/10.1021/acsenergylett.8b01562.
21. Xu, W., Hart, L.J.F., Moss, B., Caprioglio, P., Macdonald, T.J., Furlan, F., Panidi, J., Oliver, R.D.J., Pacalaj, R.A., Heeney, M., et al. (2023). Impact of Interface Energetic Alignment and Mobile Ions on Charge Carrier Accumulation and Extraction in p-i-n Perovskite Solar Cells. Adv. Energy Mater. *13*, 2301102. https://doi.org/10.1002/aenm.202301102.
22. Brinkmann, K.O., Becker, T., Zimmermann, F., Kreusel, C., Gahlmann, T., Theisen, M., Haeger, T., Olthof, S., Tückmantel, C., Günster, M., et al. (2022). Perovskite–organic tandem solar cells with indium oxide interconnect. Nature *604*, 280–286. https://doi.org/10.1038/s41586-022-04455-0.
23. Liu, J., De Bastiani, M., Aydin, E., Harrison, G.T., Gao, Y., Pradhan, R.R., Eswaran, M.K., Mandal, M., Yan, W., Seitkhan, A., et al. (2022). Efficient and stable perovskite-silicon tandem solar cells through contact displacement by MgF_x. Science *377*, 302–306. https://doi.org/10.1126/science.abn8910.
24. Hu, X., Jiang, X.-F., Xing, X., Nian, L., Liu, X., Huang, R., Wang, K., Yip, H.-L., and Zhou, G. (2018). Wide-Bandgap Perovskite Solar Cells With Large Open-Circuit Voltage of 1653 mV Through Interfacial Engineering. Sol. RRL *2*, 1800083. https://doi.org/10.1002/solr.201800083.
25. El-Hajje, G., Momblona, C., Gil-Escrig, L., Ávila, J., Guillemot, T., Guillemoles, J.-F., Sessolo, M., Bolink, H.J., and Lombez, L. (2016). Quantification of spatial inhomogeneity in perovskite solar cells by hyperspectral luminescence imaging. Energy Environ. Sci. *9*, 2286–2294. https://doi.org/10.1039/C6EE00462H.
26. Caprioglio, P., Smith, J.A., Oliver, R.D.J., Dasgupta, A., Choudhary, S., Farrar, M.D., Ramadan, A.J., Lin, Y.-H., Christoforo, M.G., Ball, J.M., et al. (2023). Open-circuit and short-circuit loss management in wide-gap perovskite p-i-n solar cells. Nat. Commun. *14*, 932. https://doi.org/10.1038/s41467-023-36141-8.
27. Al-Ashouri, A., Köhnen, E., Li, B., Magomedov, A., Hempel, H., Caprioglio, P., Márquez, J.A., Morales Vilches, A.B.M., Kasparavicius, E., Smith, J.A., et al. (2020). Monolithic perovskite/silicon tandem solar cell with >29% efficiency by enhanced hole extraction. Science *370*, 1300–1309. https://doi.org/10.1126/science.abd4016.
28. Al-Ashouri, A., Magomedov, A., Roß, M., Jošt, M., Talaikis, M., Chistiakova, G., Bertram, T., Márquez, J.A., Köhnen, E., Kasparavičius, E., et al. (2019). Conformal monolayer contacts with lossless interfaces for perovskite single junction and monolithic tandem solar cells. Energy Environ. Sci. *12*, 3356–3369. https://doi.org/10.1039/C9EE02268F.
29. Magomedov, A., Al-Ashouri, A., Kasparavičius, E., Strazdaite, S., Niaura, G., Jošt, M., Malinauskas, T., Albrecht, S., and Getautis, V. (2018). Self-Assembled Hole Transporting Monolayer for Highly Efficient Perovskite Solar Cells. Adv. Energy Mater. *8*, 1801892. https://doi.org/10.1002/aenm.201801892.
30. Lin, Y., Magomedov, A., Firdaus, Y., Kaltsas, D., El-Labban, A., Faber, H., Naphade, D.R., Yengel, E., Zheng, X., Yarali, E., et al. (2021). 18.4 % Organic Solar Cells Using a High Ionization Energy Self-Assembled Monolayer as Hole-Extraction Interlayer. ChemSusChem

14, 3569–3578. https://doi.org/10.1002/cssc.202100707.

31. Levine, I., Al-Ashouri, A., Musiienko, A., Hempel, H., Magomedov, A., Drevilkauskaite, A., Getautis, V., Menzel, D., Hinrichs, K., Unold, T., et al. (2021). Charge transfer rates and electron trapping at buried interfaces of perovskite solar cells. Joule *5*, 2915–2933. https://doi.org/10.1016/j.joule.2021.07.016.

32. Isikgor, F.H., Zhumagali, S., Merino, T., De Bastiani, M., McCulloch, I., and De Wolf, S. (2023). Molecular engineering of contact interfaces for high-performance perovskite solar cells. Nat. Rev. Mater. *8*, 89–108. https://doi.org/10.1038/s41578-022-00503-3.

33. Almasabi, K., Zheng, X., Turedi, B., Alsalloum, A.Y., Lintangpradipto, M.N., Yin, J., Gutiérrez-Arzaluz, L., Kotsovos, K., Jamal, A., Gereige, I., et al. (2023). Hole-Transporting Self-Assembled Monolayer Enables Efficient Single-Crystal Perovskite Solar Cells with Enhanced Stability. ACS Energy Lett. *8*, 950–956. https://doi.org/10.1021/acsenergylett.2c02333.

34. Mishima, R., Hino, M., Kanematsu, M., Kishimoto, K., Ishibashi, H., Konishi, K., Okamoto, S., Irie, T., Fujimoto, T., Yoshida, W., et al. (2022). 28.3% efficient perovskite-silicon tandem solar cells with mixed self-assembled monolayers. Appl. Phys. Express *15*, 076503. https://doi.org/10.35848/1882-0786/ac727b.

35. Li, L., Wang, Y., Wang, X., Lin, R., Luo, X., Liu, Z., Zhou, K., Xiong, S., Bao, Q., Chen, G., et al. (2022). Flexible all-perovskite tandem solar cells approaching 25% efficiency with molecule-bridged hole-selective contact. Nat. Energy *7*, 708–717. https://doi.org/10.1038/s41560-022-01045-2.

36. Aydin, E., Ugur, E., Yildirim, B.K., Allen, T.G., Dally, P., Razzaq, A., Cao, F., Xu, L., Vishal, B., Yazmaciyan, A., et al. (2023). Enhanced optoelectronic coupling for perovskite/silicon tandem solar cells. Nature *623*, 732–738. https://doi.org/10.1038/s41586-023-06667-4.

37. Mariotti, S., Köhnen, E., Scheler, F., Sveinbjörnsson, K., Zimmermann, L., Piot, M., Yang, F., Li, B., Warby, J., Musiienko, A., et al. (2023). Interface engineering for high-performance, triple-halide perovskite–silicon tandem solar cells. Science *381*, 63–69. https://doi.org/10.1126/science.adf5872.

38. Lin, R., Xu, J., Wei, M., Wang, Y., Qin, Z., Liu, Z., Wu, J., Xiao, K., Chen, B., Park, S.M., et al. (2022). All-perovskite tandem solar cells with improved grain surface passivation. Nature *603*, 73–78. https://doi.org/10.1038/s41586-021-04372-8.

39. Xu, H., Torres Merino, L., Koc, M., Aydin, E., Zhumagali, S., Haque, M.A., Yazmaciyan, A., Sharma, A., Rosas Villalva, D., Huerta Hernandez, L., et al. (2022). Metal-Free Interconnecting Layer for Monolithic Perovskite/Organic Tandem Solar Cells with Enhanced Outdoor Stability. ACS Appl. Energy Mater. *5*, 14035–14044. https://doi.org/10.1021/acsaem.2c01749.

40. Wang, Z., Zeng, L., Zhu, T., Chen, H., Chen, B., Kubicki, D.J., Balvanz, A., Li, C., Maxwell, A., Ugur, E., et al. (2023). Suppressed phase segregation for triple-junction perovskite solar cells. Nature *618*, 74–79. https://doi.org/10.1038/s41586-023-06006-7.

41. Isikgor, F.H., Maksudov, T., Chang, X., Adilbekova, B., Ling, Z., Hadmojo, W.T., Lin, Y., and Anthopoulos, T.D. (2022). Monolithic Perovskite–Perovskite–Organic Triple-Junction Solar Cells with a Voltage Output Exceeding 3 V. ACS Energy Lett. *7*, 4469–4471. https://doi.org/10.1021/acsenergylett.2c02340.

42. Zheng, J., Wang, G., Duan, W., Mahmud, M.A., Yi, H., Xu, C., Lambertz, A., Bremner, S., Ding, K., Huang, S., et al. (2022). Monolithic Perovskite–Perovskite–Silicon Triple-Junction Tandem Solar Cell with an Efficiency of over 20%. ACS Energy Lett. *7*, 3003–3005. https://doi.org/10.1021/acsenergylett.2c01556.

43. Ma, C., Eickemeyer, F.T., Lee, S.-H., Kang, D.-H., Kwon, S.J., Grätzel, M., and Park, N.-G. (2023). Unveiling facet-dependent degradation and facet engineering for stable perovskite solar cells. Science *379*, 173–178. https://doi.org/10.1126/science.adf3349.

44. Ma, C., Grätzel, M., and Park, N.-G. (2022). Facet Engineering for Stable, Efficient Perovskite Solar Cells. ACS Energy Lett. *7*, 3120–3128. https://doi.org/10.1021/acsenergylett.2c01623.

45. Ma, C., Kang, M.-C., Lee, S.-H., Kwon, S.J., Cha, H.-W., Yang, C.-W., and Park, N.-G. (2022). Photovoltaically top-performing perovskite crystal facets. Joule *6*, 2626–2643. https://doi.org/10.1016/j.joule.2022.09.012.

46. Krogmeier, B., Staub, F., Grabowski, D., Rau, U., and Kirchartz, T. (2018). Quantitative analysis of the transient photoluminescence of $CH_3NH_3PbI_3/PC_{61}BM$ heterojunctions by numerical simulations. Sustainable Energy Fuels *2*, 1027–1034.

47. Oliver, R.D.J., Caprioglio, P., Peña-Camargo, F., Buizza, L.R.V., Zu, F., Ramadan, A.J., Motti, S.G., Mahesh, S., McCarthy, M.M., Warby, J.H., et al. (2022). Understanding and suppressing non-radiative losses in methylammonium-free wide-bandgap perovskite solar cells. Energy Environ. Sci. *15*, 714–726. https://doi.org/10.1039/D1EE02650J.

48. Ma, K., Atapattu, H.R., Zhao, Q., Gao, Y., Finkenauer, B.P., Wang, K., Chen, K., Park, S.M., Coffey, A.H., Zhu, C., et al. (2021). Multifunctional Conjugated Ligand Engineering for Stable and Efficient Perovskite Solar Cells. Adv. Mater. *33*, e2100791. https://doi.org/10.1002/adma.202100791.

49. Wang, H., Chen, Z., Hu, J., Yu, H., Kuang, C., Qin, J., Liu, X., Lu, Y., Fahlman, M., Hou, L., et al. (2021). Dynamic Redistribution of Mobile Ions in Perovskite Light-Emitting Diodes. Adv. Funct. Mater. *31*, 2007596. https://doi.org/10.1002/adfm.202007596.

50. Babics, M., De Bastiani, M., Ugur, E., Xu, L., Bristow, H., Toniolo, F., Raja, W., Subbiah, A.S., Liu, J., Torres Merino, L.V., et al. (2023). One-year outdoor operation of monolithic perovskite/silicon tandem solar cells. Cell Rep. Phys. Sci. *4*, 101280. https://doi.org/10.1016/j.xcrp.2023.101280.

51. Babbe, F., Masquelier, E., Zheng, Z., and Sutter-Fella, C.M. (2020). Flash Formation of I-Rich Clusters during Multistage Halide Segregation Studied in $MAPbI_{1.5}Br_{1.5}$. J. Phys. Chem. C *124*, 24608–24615. https://doi.org/10.1021/acs.jpcc.0c07063.

52. Suchan, K., Just, J., Beblo, P., Rehermann, C., Merdasa, A., Mainz, R., Scheblykin, I.G., and Unger, E. (2023). Multi-Stage Phase-Segregation of Mixed Halide Perovskites under Illumination: A Quantitative Comparison of Experimental Observations and Thermodynamic Models. Adv. Funct. Mater. *33*, 2206047. https://doi.org/10.1002/adfm.202206047.

53. Thiesbrummel, J., Le Corre, V.M., Peña-Camargo, F., Perdigón-Toro, L., Lang, F., Yang, F., Grischek, M., Gutierrez-Partida, E., Warby, J., Farrar, M.D., et al. (2021). Universal Current Losses in Perovskite Solar Cells Due to Mobile Ions. Adv. Energy Mater. *11*, 2101447. https://doi.org/10.1002/aenm.202101447.

54. Thiesbrummel, J., Shah, S., Gutierrez-Partida, E., Zu, F., Peña-Camargo, F., Zeiske, S., Diekmann, J., Ye, F., Peters, K.P., Brinkmann, K.O., et al. (2024). Ion-induced field screening as a dominant factor in perovskite solar cell operational stability. Nat. Energy *9*, 664–676. https://doi.org/10.1038/s41560-024-01487-w.

55. Diekmann, J., Caprioglio, P., Futscher, M.H., Le Corre, V.M., Reichert, S., Jaiser, F., Arvind, M., Toro, L.P., Gutierrez-Partida, E., Peña-Camargo, F., et al. (2021). Pathways toward 30% Efficient Single-Junction Perovskite Solar Cells and the Role of Mobile Ions. Sol. RRL *5*, 2100219. https://doi.org/10.1002/solr.202100219.

56. Diekmann, J., Peña-Camargo, F., Tokmoldin, N., Thiesbrummel, J., Warby, J., Gutierrez-Partida, E., Shah, S., Neher, D., and Stolterfoht, M. (2023). Determination of Mobile Ion Densities in Halide Perovskites via Low-Frequency Capacitance and Charge Extraction Techniques. J. Phys. Chem. Lett. *14*, 4200–4210. https://doi.org/10.1021/acs.jpclett.3c00530.

57. Aeberhard, U., Altazin, S., Stepanova, L., Stous, A., Blülle, B., Kirsch, C., Knapp, E., and Ruhstaller, B. (2019). Numerical Optimization of Organic and Hybrid Multijunction Solar Cells. 2019 IEEE 46th Photovoltaic Specialists Conference (PVSC), 105–111.

58. Xu, Z., Astridge, D.D., Kerner, R.A., Zhong, X., Hu, J., Hong, J., Wisch, J.A., Zhu, K., Berry, J.J., Kahn, A., et al. (2023). Origins of Photoluminescence Instabilities at Halide Perovskite/Organic Hole Transport Layer Interfaces. J. Am. Chem. Soc. *145*, 11846–11858. https://doi.org/10.1021/jacs.3c03539.

59. Le Corre, V.M., Diekmann, J., Peña-Camargo, F., Thiesbrummel, J., Tokmoldin, N., Gutierrez-Partida, E., Peters, K.P., Perdigón-Toro, L., Futscher, M.H., Lang, F., et al. (2022). Quantification of Efficiency Losses Due to Mobile Ions in Perovskite Solar Cells via Fast Hysteresis Measurements. Sol. RRL *6*, 2100772. https://doi.org/10.1002/solr.202100772.

60. Azmi, R., Utomo, D.S., Vishal, B., Zhumagali, S., Dally, P., Risqi, A.M., Prasetio, A., Ugur, E., Cao, F., Imran, I.F., et al. (2024). Double-side 2D/3D heterojunctions for inverted perovskite solar cells. Nature *628*, 93–98. https://doi.org/10.1038/s41586-024-07189-3.

61. Aydin, E., Liu, J., Ugur, E., Azmi, R., Harrison, G.T., Hou, Y., Chen, B., Zhumagali, S., De Bastiani, M., Wang, M., et al. (2021). Ligand-bridged charge extraction and enhanced quantum efficiency enable efficient n–i–p perovskite/silicon tandem solar cells. Energy Environ. Sci. *14*, 4377–4390. https://doi.org/10.1039/D1EE01206A.

62. Frisch, M.J., Trucks, G., Schlegel, H.B., Scuseria, G.E., Robb, M.A., Cheeseman, J.R., Scalmani, G., Barone, V., Mennucci, B., Petersson, G.A., et al. (2009). Gaussian 09 (Gaussian Inc.).

63. Kirchartz, T., Márquez, J.A., Stolterfoht, M., and Unold, T. (2020). Photoluminescence-Based Characterization of Halide Perovskites for Photovoltaics. Adv. Energy Mater. *10*, 1904134. https://doi.org/10.1002/aenm.201904134.

64. Mooney, J., and Kambhampati, P. (2013). Get the Basics Right: Jacobian Conversion of Wavelength and Energy Scales for Quantitative Analysis of Emission Spectra. J. Phys. Chem. Lett. *4*, 3316–3318. https://doi.org/10.1021/jz401508t.

65. Dittrich, T., and Fengler, S. (2019). Surface photovoltage analysis of photoactive materials (World Scientific).